



Measurement of statistical nuclear spin polarization in a nanoscale GaAs sample

Fei Xue (薛飞), D. P. Weber, P. Peddibhotla, and M. Poggio

Department of Physics, University of Basel, Klingelbergstrasse 82, CH-4056 Basel, Switzerland

(Received 2 September 2011; revised manuscript received 21 October 2011; published 21 November 2011)

We measure the statistical polarization of quadrupolar nuclear spins in a submicrometer ($0.6 \mu\text{m}^3$) particle of GaAs using magnetic resonance force microscopy. The crystalline sample is cut out of a GaAs wafer and attached to a micromechanical cantilever force sensor using a focused ion beam technique. Nuclear magnetic resonance is demonstrated on ensembles containing less than 5×10^8 nuclear spins and occupying a volume of around $(300 \text{ nm})^3$ in GaAs with reduced volumes possible in future experiments. We discuss how the further reduction of this detection volume will bring the spin ensembles into a regime where random spin fluctuations, rather than Boltzmann polarization, dominate their dynamics. The detection of statistical polarization in GaAs therefore represents an important first step toward 3D magnetic resonance imaging of III-V structures on the nanometer scale.

DOI: [10.1103/PhysRevB.84.205328](https://doi.org/10.1103/PhysRevB.84.205328)

PACS number(s): 76.70.-r, 05.40.-a, 68.37.Rt, 85.85.+j

I. INTRODUCTION

Recent years have seen the development of a wide range of semiconducting nanostructures including quantum wells (QWs), nanowires (NWs), and quantum dots (QDs). Researchers have devoted particular attention to making devices from III-V materials such as GaAs, whose high electron mobility and direct band gap make it a critical component of today's semiconductor technology. III-V systems are extremely versatile in large part due to techniques such as molecular-beam epitaxy (MBE) and metal-organic chemical vapor deposition (MOCVD), which enable the growth of complex heterostructures with nearly perfect crystalline interfaces. As a result, applications range from integrated circuits operating at microwave frequencies to light-emitting and laser diodes to quantum structures used for basic research.

While a variety of techniques exist to characterize and image these nanostructures, including scanning electron microscopy (SEM), tunneling electron microscopy (TEM), and x-ray crystallography, so far it has been impossible to measure single nanostructures using magnetic resonance imaging (MRI). In larger structures, MRI is a powerful technique allowing for the three-dimensional (3D), subsurface imaging of the density of particular nuclear magnetic moments. However, conventional nuclear magnetic resonance (NMR) techniques, in which the spin signal is detected by an inductive pickup coil, are limited to detection volumes of several μm on a side or larger.¹ A net polarization of at least 10^{12} nuclear spins is typically needed to generate a detectable signal; nanometer-scale samples simply do not contain enough spins to be detected. In the past few years, a more sensitive force-detected version of MRI has been demonstrated on nanometer-scale samples.² Using magnetic resonance force microscopy (MRFM) to measure the statistical polarization of spin-1/2 ^1H , Degen *et al.* made 3D images of single-virus particles with a resolution better than 10 nm .³

Here we take a step toward applying this technique to quadrupolar (spin-3/2) nuclei, specifically Ga and As, in a nanometer-scale particle. We demonstrate the detection of statistical polarizations of ^{69}Ga , ^{71}Ga , and ^{75}As in a $0.6 \mu\text{m}^3$ particle of crystalline GaAs. The mechanical detection of NMR in GaAs was first demonstrated in 2002 by

Verhagen *et al.* and Thurber *et al.*^{4,5} The smallest reported detection volume of $600 \mu\text{m}^3$ contained more than 10^{12} nuclear moments.⁶ In 2004, Garner *et al.* reported forced-detected NMR signal from 10^{10} moments in a GaAs wafer.⁷ Those experiments measured either the thermal equilibrium polarization or an optically enhanced polarization of Ga and As spins. Our experiment has a detection volume of about $0.03 \mu\text{m}^3 \approx (300 \text{ nm})^3$ equivalent to less than 5×10^8 spins of any one of the constituent isotopes. Such a volume is far too tiny to detect via conventional, inductively detected magnetic resonance, although the number of spins is not yet small enough that its polarization is dominated by statistical fluctuations. Future reductions in detection volume, however, will enter this regime and will require techniques like the one demonstrated here.

II. BOLTZMANN VS STATISTICAL POLARIZATION

Conventional magnetic resonance signals originate from the mean polarization of nuclear spins in an external magnetic field—the so-called Boltzmann polarization. Although this polarization is quite small, it dominates the spin signal for large ensembles of nuclear spins. As the size of the spin ensemble decreases, the amplitude of the polarization fluctuations eventually exceeds the mean polarization.⁸ This variance, sometimes called the statistical polarization, then becomes a more useful signal for MRI than the mean polarization.

Statistical polarization arises from the incomplete cancellation of randomly oriented spins. For any given direction, the net polarization can be either positive or negative and will fluctuate on a time scale that depends on the flip rate of the spins. Several MRFM experiments have detected statistical polarizations of spin-1/2 nuclear spins^{9–14} and demonstrated their use for nanometer-scale nuclear MRI.^{3,15}

In order to understand the regimes in which either Boltzmann or statistical polarization is important, consider an ensemble of N spins with spin quantum number I . The Hamiltonian of a single spin in the presence of a magnetic field B along \hat{z} is $\hat{H} = -\hat{\mu}_z B = -\hbar\gamma B \hat{I}_z$ where $\hat{\mu}_z$ is the magnetic dipole moment operator along \hat{z} , \hbar is Planck's constant, γ is the gyromagnetic ratio, and \hat{I}_z is the nuclear spin angular momentum operator along \hat{z} . Statistical mechanics predicts the

equilibrium distribution at a temperature T to be a Boltzmann distribution. The partition function $Z = \text{Tr}\{\exp(-\frac{\hat{H}}{k_B T})\}$ contains all the information about the nuclear spin polarization in the system, where k_B is the Boltzmann constant.¹⁶ The density matrix $\hat{\rho} = \frac{1}{Z} \exp(-\frac{\hat{H}}{k_B T})$ of the spin system can be used to compute the mean $M_z = N \text{Tr}\{\hat{\mu}_z \hat{\rho}\}$ and the variance $\sigma_{M_z}^2 = N(\text{Tr}\{\hat{\mu}_z^2 \hat{\rho}\} - (\text{Tr}\{\hat{\mu}_z \hat{\rho}\})^2)$ of the ensemble's magnetization along \hat{z} . Even at cryogenic temperatures ($T \sim 1$ K) and high magnetic fields ($B \sim 10$ T), $\hbar\gamma B \ll k_B T$. Therefore, keeping terms only up to first order in $\frac{\hbar\gamma B}{k_B T}$, we find

$$M_z = N \frac{I(I+1)}{3} \hbar\gamma \left(\frac{\hbar\gamma B}{k_B T} \right), \quad (1)$$

$$\sigma_{M_z}^2 = N \frac{I(I+1)}{3} (\hbar\gamma)^2. \quad (2)$$

Since $N\hbar\gamma I$ corresponds to 100% spin polarization, one can define the statistical nuclear polarization as $SNP = \frac{\sigma_{M_z}}{N\hbar\gamma I} = \sqrt{\frac{I+1}{3I} \frac{1}{N}}$ and the Boltzmann nuclear polarization as $BNP = \frac{M_z}{N\hbar\gamma I} = \frac{I+1}{3} \frac{\hbar\gamma B}{k_B T}$. Statistical polarization dominates the system ($SNP > BNP$) when the number of spins in an ensemble is less than the critical number,

$$N_c = \frac{3}{I(I+1)} \left(\frac{k_B T}{\hbar\gamma B} \right)^2. \quad (3)$$

Equivalently, for a material with a nuclear spin density na , where n is the number density of the nuclear element and a is the natural abundance of the isotope of interest, one can define a critical volume $V_c = \frac{N_c}{na}$. For volumes smaller than V_c , magnetic resonance experiments should be designed to detect SNP rather than BNP .

III. MRFM TECHNIQUE AND APPARATUS

We measure the presence of a particular nuclear isotope using a MRFM protocol which cyclically inverts statistical spin polarization.¹⁵ In a magnetic field $\mathbf{B}_{\text{total}}$, the frequency of a transverse RF magnetic field \mathbf{B}_1 is swept through the nuclear resonance condition, $f_{\text{RF}} = \frac{\gamma}{2\pi} B_{\text{total}}$. If done adiabatically, this sweep induces the nuclear spins to invert—a process known as adiabatic rapid passage. In the strong spatial magnetic field gradient near a magnetic tip, these inversions produce a time-dependent force. This force is in turn detected as the displacement of an ultrasensitive cantilever.

Our MRFM experiment is carried out in a sample-on-cantilever configuration in which the sample is affixed to the end of a single-crystal Si cantilever¹⁷ as shown in Fig. 1. We arrange the cantilever in a “pendulum” geometry such that the sample is positioned above a FeCo magnetic tip, depicted in Fig. 2. The magnetic tip, which is mounted on a separate chip, is patterned on top of an Au microwire, which acts as an RF magnetic field source and is shown in Fig. 3.¹⁰

The cantilever measures $120 \mu\text{m} \times 4 \mu\text{m} \times 0.1 \mu\text{m}$ and—loaded with the GaAs sample—has a mechanical resonance frequency $f_c = \omega_c/(2\pi) = 3.7$ kHz and an intrinsic quality factor $Q = 4.0 \times 10^4$ at $T = 1$ K. By measuring the cantilever's thermal motion, we determine its effective spring constant to be $k = 120 \mu\text{N/m}$. The MRFM apparatus is isolated from

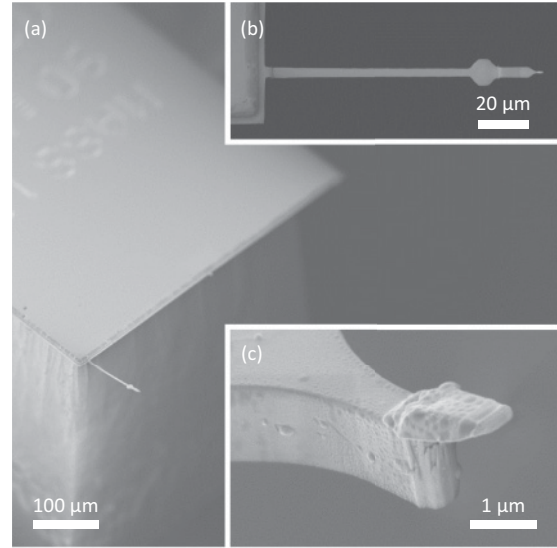


FIG. 1. SEM micrograph of the Si cantilever with a GaAs sample attached. (A) shows the cantilever protruding from a Si chip. (B) clarifies the geometry showing the paddle and mass-loaded end of the cantilever, and (C) is a detailed view of the tip of the mass-loaded cantilever with the GaAs sample attached. A layer of Pt is visible at the very tip of the GaAs particle.

vibrational noise and is mounted in a vacuum chamber with a pressure below 10^{-6} mbar at the bottom of a ^3He cryostat. The motion of the lever is detected using 100 nW of 1550 nm laser light focused onto a 12- μm -wide paddle and reflected back into an optical fiber interferometer. The microwire used to produce the transverse RF magnetic field is 2.5 μm long,

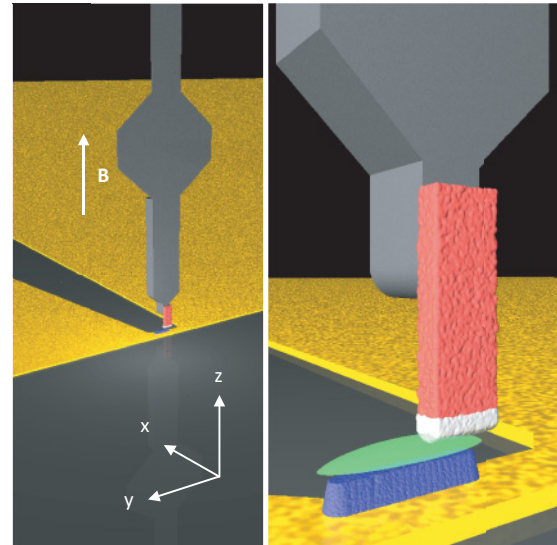


FIG. 2. (Color) Representation of the MRFM apparatus at the bottom of the cryostat. The microwire is shown in yellow, the FeCo tip in blue, and the GaAs sample in red, with a Pt layer on its end in white. The green region above the FeCo tip depicts the resonant slice during measurement. \mathbf{B} , the cantilever shaft, and the magnetization of the FeCo tip are aligned along \hat{z} . Near the FeCo tip, current flows in the wire along \hat{y} , while the lever displacement and \mathbf{B}_1 at the position of the sample are directed along \hat{x} .

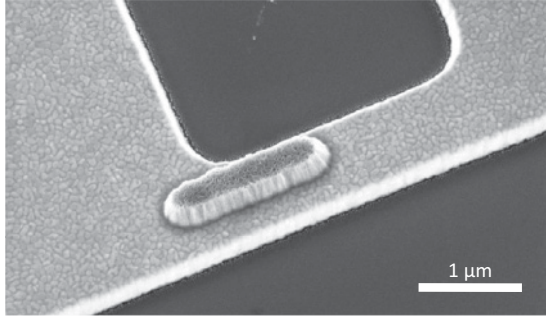


FIG. 3. SEM micrograph of the Au microwire with integrated FeCo tip. The structure is patterned on a Si chip.

1 μm wide, and 0.2 μm thick. The FeCo tip is shaped like a bar, sits on top of the microwire, and produces a spatially dependent field $\mathbf{B}_{\text{tip}}(\vec{r})$. It has a top width of 270 nm, a bottom width of 510 nm, a length of 1.2 μm , and a height of 265 nm, as shown in Fig. 3. To make sure that the FeCo tip is fully magnetized along \hat{z} , an external magnetic field $\mathbf{B} = B\hat{z}$ is applied with $B = 2.65$ T. During measurements, the distance between the FeCo tip and the closest point on the sample is typically 100 nm such that the static magnetic field gradient $\frac{\partial B_{\text{total}}}{\partial x}$ relevant to MRFM is on the order of 5×10^5 T/m, where $\mathbf{B}_{\text{total}} = \mathbf{B} + \mathbf{B}_{\text{tip}}$ and \hat{x} is the direction of cantilever oscillation. The maximum $|\mathbf{B}_{\text{tip}}|$ for this spacing is about 0.1 T. Smaller spacings can result in larger $\frac{\partial B_{\text{total}}}{\partial x}$ and $|\mathbf{B}_{\text{tip}}|$, although they also result in larger measurement noise. Interactions between the magnetic tip and the sample at such small gaps, known as noncontact friction, lead to mechanical dissipation in the cantilever.^{18,19} In our experiments, these effects reduce the quality factor Q of the cantilever to 1.0×10^4 . In addition, we damp Q down to ~ 400 using active electronic feedback.²⁰ Given the narrow natural bandwidth of our high- Q cantilever, damping is used to increase the bandwidth of our force detection without sacrificing signal-to-noise ratio (SNR).²¹

If the rate of the RF frequency sweeps used to invert the nuclear spins is slow enough and the amplitude of B_1 large enough, the initial population distribution among the nuclear spin energy levels is completely inverted. As a result, net magnetization is made to flip along the \hat{z} . For spin-1/2 nuclei, the criterion for adiabatic inversion is given by $\alpha = 2\pi\gamma^2 B_1^2 / (\omega_c \Omega_{\text{RF}}) \gg 1$, where $\Omega_{\text{RF}} / (2\pi)$ is the amplitude of the frequency modulation around the center frequency f_{RF} of the transverse RF field B_1 .¹⁶ The criterion for quadrupolar nuclei, in general, is more complex.²² However, a complete inversion of the initial population distribution over the quadrupolar energy levels can be achieved in the limit of both $\alpha \gg 1$ and $\beta = \gamma B_1 / \Omega_Q \gg 1$, where $\Omega_Q / (2\pi)$ is the quadrupolar frequency. The frequency sweeps used here are designed to meet these conditions and follow the form used in Poggio *et al.*¹⁰ Therefore, by sweeping through f_{RF} at a frequency $2f_c$, we are able to modulate the spin polarization at f_c . The resulting spin inversions produce a force that drives the cantilever at its resonance frequency. An ensemble of spins at position \vec{r} with a statistical variance in its magnetization $\sigma_{M_z}^2$ produces a force on the cantilever with variance,

$$\sigma_F^2 = \left(\frac{\partial B_{\text{total}}}{\partial x}(\vec{r}) \right)^2 \sigma_{M_z}^2. \quad (4)$$

Using our knowledge of the spring constant k , we determine σ_F^2 by measuring the variance of the cantilever's oscillations on resonance. The correlation time τ_m of σ_F^2 is limited by the relaxation rate of the spins in the rotating frame.

IV. RECEPTIVITY IN MRFM OF STATISTICALLY POLARIZED ENSEMBLES

Due to differences in magnetic moment and statistical polarization, two ensembles containing the same number of nuclei but each of a different isotope, produce different magnetization variances. This difference is contained within the concept of receptivity. Receptivity is a value defined for the purpose of comparing the expected NMR signal magnitudes for equal numbers of different nuclear isotopes. For MRFM of statistically polarized ensembles, we define a receptivity $R_{N,\text{MRFM}} \propto \gamma^2 I(I+1)$, where $R_{N,\text{MRFM}}$ is normalized to 1 for ^1H . The factor $\gamma^2 I(I+1)$ is proportional to the magnetization variance expected from an ensemble of spins as defined in (2). From (4), the variance multiplied by the square of the magnetic field gradient results in the resonant force variance measured in MRFM.

On the other hand, conventional NMR collects an inductive signal due to a Boltzmann polarization. In this case, receptivity can be defined as $R_{N,\text{conv}} \propto \gamma^3 I(I+1)$, where $R_{N,\text{conv}}$ is similarly normalized to 1 for ^1H . Here the factor $\gamma^2 I(I+1)$ is proportional to the Boltzmann polarization as defined in (1). The remaining factor of γ results from the fact that conventional NMR measures the inductive response of a pickup coil to magnetization precessing at a frequency proportional to γ .²³

As can be noted in Table I, MRFM receptivity scales more favorably than conventional receptivity for low- γ nuclei such as those found in GaAs. In real experiments, comparisons are often made between signals from two different isotopes contained in the same volume. In the comparison of volumes rather than number of nuclei, one must also take into account the number density n of each element in the material and its natural isotopic abundance a . Volume receptivity therefore also includes the factors of n and a : $R_{V,\text{MRFM}} \propto naR_{N,\text{MRFM}}$ and $R_{V,\text{conv}} \propto naR_{N,\text{conv}}$.

V. MRFM MEASUREMENTS

Here we study a submicron-sized particle cut from the surface of a GaAs wafer. The GaAs sample is affixed to the cantilever tip using a focused ion beam (FIB) technique. First, a thin layer of Pt is deposited over a small area of a GaAs wafer to protect the sample from potential ion damage. Then, a lamella measuring $3 \mu\text{m} \times 2 \mu\text{m} \times 0.3 \mu\text{m}$ is cut out from this area of the wafer. Next, the lamella is welded with Pt to a nearby micromanipulator and transferred to the tip of an ultrasensitive Si cantilever. Finally, the particle is Pt-welded to the cantilever tip and cut to its final dimensions: $2.4 \mu\text{m} \times 0.8 \mu\text{m} \times 0.3 \mu\text{m} = 0.6 \mu\text{m}^3$ (Fig. 1). The side of the sample which formerly was part of the wafer surface is oriented such that it faces away from the cantilever. A roughly 200-nm-thick layer of the original Pt protection layer remains on this surface of the particle.²⁴ Throughout this process, only the mass-loaded end of the cantilever is exposed to either the

TABLE I. Properties relevant for a statistically polarized MRFM measurement.

| | ^1H (hydrocarbon layer) | ^{69}Ga (GaAs) | ^{71}Ga (GaAs) | ^{75}As (GaAs) |
|----------------------------------|-------------------------------------|----------------------------|----------------------------|----------------------------|
| I | 1/2 | 3/2 | 3/2 | 3/2 |
| $\frac{\gamma}{2\pi}$ (MHz/T) | 42.57 | 10.3 | 13.0 | 7.3 |
| a | 1.000 | 0.601 | 0.399 | 1.000 |
| n (m^{-3}) | 7×10^{28} | 2.2×10^{28} | 2.2×10^{28} | 2.2×10^{28} |
| N_c ($B = 2.65$ T, $T = 1$ K) | 1.4×10^5 | 4.7×10^5 | 2.9×10^5 | 9.3×10^5 |
| V_c ($B = 2.65$ T, $T = 1$ K) | $(12 \text{ nm})^3$ | $(33 \text{ nm})^3$ | $(32 \text{ nm})^3$ | $(35 \text{ nm})^3$ |
| $R_{N,\text{MRFM}}$ | 1 | 0.293 | 0.466 | 0.147 |
| $R_{N,\text{conv}}$ | 1 | 0.071 | 0.142 | 0.025 |
| $R_{V,\text{MRFM}}$ | 1 | 0.056 | 0.058 | 0.046 |
| $R_{V,\text{conv}}$ | 1 | 0.013 | 0.018 | 0.008 |

ion or electron beams. Special care is taken never to expose the cantilever shaft in order to avoid structural damage or deposition of material on its surface. Even short exposure can lead to the permanent bending of the cantilever and a reduction of its mechanical Q .

MRFM signal measured from this GaAs particle at $B = 2.65$ T and temperature $T = 1$ K is plotted as a function of the RF center frequency in Fig. 4. Resonances from all three isotopes (^{69}Ga , ^{71}Ga , and ^{75}As) in GaAs are visible. In addition, a strong ^1H resonance appears in the spectrum due to the thin layer of adsorbed hydrocarbons and water that coats surfaces which have been exposed to ordinary laboratory air.^{3,15} Each resonance is measured with the GaAs particle

positioned at slightly different x and y positions in the vicinity of the FeCo tip. In each case, however, the spacing along \hat{z} between the end of the particle and the top of the FeCo tip is 100 nm. Similar magnitudes of B_1 are used in each case, which we quantify in the discussion of Fig. 5. The frequency modulation amplitude $\Omega_{\text{RF}}/(2\pi)$ is 400 kHz for ^1H , 100 kHz for ^{69}Ga and ^{71}Ga , and 50 kHz for ^{75}As . Each data point represents 300 s of averaging for ^1H , 600 s for ^{69}Ga and ^{71}Ga , and 1400 s for ^{75}As . While the SNR for some peaks is small— ^{75}As and ^{69}Ga in particular—each peak is confirmed by at least one other experiment performed at a different magnetic field B . The appropriate shift in carrier frequency is observed in each case.

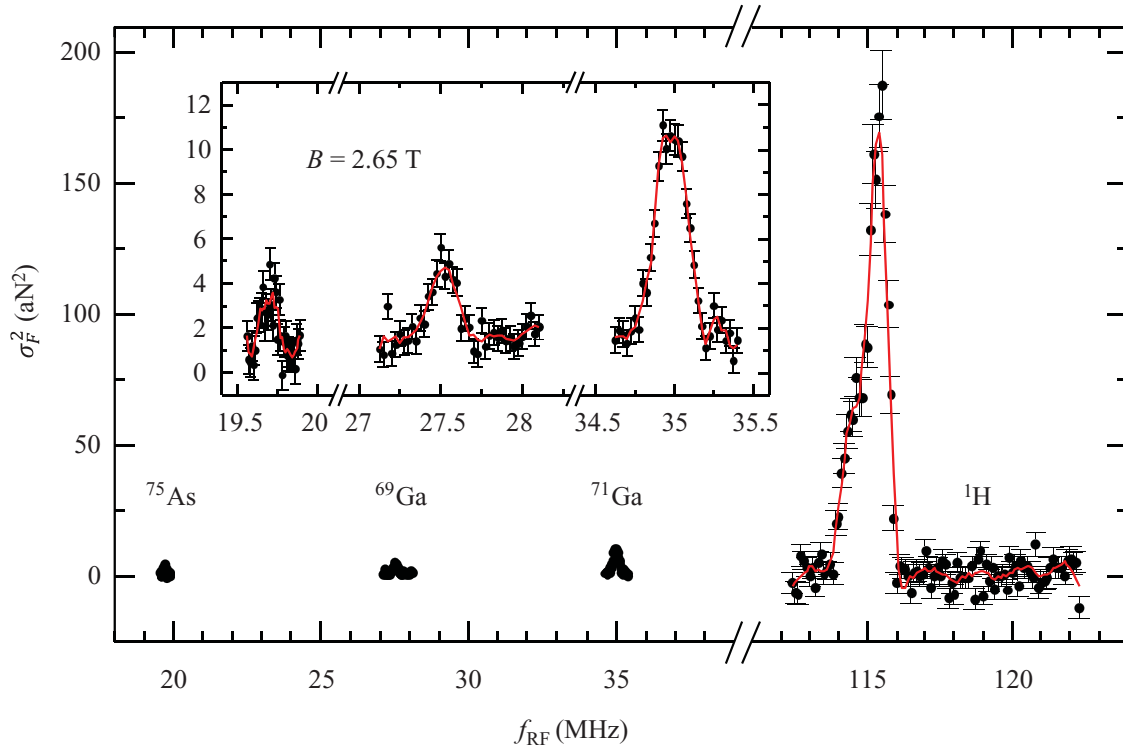


FIG. 4. (Color online) MRFM signal from the statistical polarization of ^1H , ^{69}Ga , ^{71}Ga , and ^{75}As . Black dots show the resonant force variance σ_F^2 as a function of the center frequency f_{RF} . Solid red lines represent adjacent-averaging of the data as a guide to the eye. Inset is a zoomed-in view of the spin-3/2 nuclear resonances: ^{69}Ga , ^{71}Ga , and ^{75}As . Error bars represent the standard error of σ_F^2 calculated as in Degen *et al.* (Ref. 11). Data points represent 1400 s of averaging for ^{75}As , 600 s for ^{69}Ga , 600 s for ^{71}Ga , and 300 s for ^1H .

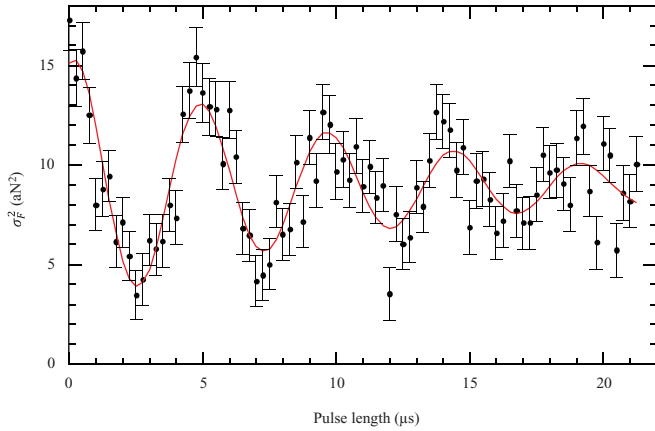


FIG. 5. (Color online) Nutation measurement for ^{71}Ga at $T = 1$ K. σ_F^2 from ^{71}Ga spins is measured as a function of pulse length. A rotating-frame RF magnetic field amplitude B_1 of 16 mT is obtained from a decaying sinusoidal fit (shown in red) to the Rabi oscillations. Error bars represent the standard error of σ_F^2 calculated as in Degen *et al.* (Ref. 11).

The rotating-frame spin correlation time τ_m observed for ^1H is on the order of 100 ms, which is consistent with spin correlation times measured in similar experiments on surface hydrocarbon layers.^{3,15} For the quadrupolar isotopes in GaAs, we measure τ_m to be around 500 ms. Thurber *et al.* report τ_m on the order of several seconds in MRFM measurements of Boltzmann polarized quadrupolar spins in a GaAs wafer.⁶ Given that the adiabaticity parameter α is similar to that used in our experiments, the difference in τ_m is likely due to the large difference in magnetic field gradient in the two cases. Gradients in our experiments exceed 10^5 T/m while gradients used by Thurber *et al.* are 100 times smaller. High magnetic field gradients on this order have been shown to limit τ_m in similar MRFM experiments.¹² In particular, mechanical noise originating from the thermal motion of the cantilever couples through strong magnetic field gradients to produce nuclear spin relaxation in the statistically polarized ensemble.

The central frequency, amplitude, and width of the resonance peaks depend on the various experimental parameters including γ , B , the spatial dependence of B_{tip} , the shape of the sample, its position relative to the FeCo tip, and the form of the adiabatic sweep wave form. Roughly, however, one can say that the low-frequency onset of each resonance should occur at $\frac{\gamma}{2\pi}B$. Note that the peak magnitudes in Fig. 4 do not scale with $R_{\text{V,MRFM}}$ since both the volume of the material detected and the magnetic field gradient in that volume are different for each measured peak. The striking difference in signal amplitude between the hydrocarbon layer and the quadrupolar nuclei in the GaAs particle is mostly due to the smaller gradients present inside the GaAs particle compared to those present at the hydrocarbon layer. Due to the 200 nm Pt layer covering the tip of the GaAs particle, the ^1H -containing layer is 200 nm closer to the FeCo tip than any of the isotopes in GaAs. As a result, for the same sample tip-sample spacing, the ^1H nuclei experience about ten times higher $\frac{\partial B_{\text{total}}}{\partial x}$ than the quadrupolar isotopes—resulting in force variances 100 times larger from the same magnetization. We

discuss the effect of each parameter on the resonances in more detail in Sec. VII.

VI. NUTATION MEASUREMENTS

Using the method described in Poggio *et al.*,¹⁰ we also measure the rotating-frame amplitude of B_1 . Pulses of variable length are inserted in the adiabatic sweep wave form every 500 cantilever cycles (135 ms). The measured force variance in spin nutation experiments of ^{71}Ga is plotted in Fig. 5 for a spacing along \hat{z} between sample and FeCo tip of 100 nm. The amplitude of the rotating RF magnetic field is inferred by fitting the data to a decaying sinusoid. The frequency of the sinusoid corresponds to the Rabi frequency γB_1 of the isotope in question and the decay rate is related to the spatial inhomogeneity of B_{tip} within the detection volume. The measured Rabi frequency of 208 kHz for ^{71}Ga corresponds to $B_1 = 16$ mT. This measurement represents the rotating-frame amplitude B_1 in the region of the GaAs particle closest to the FeCo tip, where the gradients and the resulting contribution to the MRFM signal are largest. Similar nutation measurements done using the ^1H containing layer, which is 200 nm closer to the FeCo tip, result in $B_1 = 17$ mT. This larger measured value results from the small increase in B_1 experienced as one approaches the RF microwire source.

We calculate the Rabi frequencies at $B_1 = 16$ mT for the remaining isotopes to be 680 kHz for ^1H , 165 kHz for ^{69}Ga , and 117 kHz for ^{75}As . All isotopes satisfy the adiabaticity condition $\alpha \gg 1$. Due to cubic symmetry, no quadrupolar splitting should be present in crystalline GaAs. A small amount of strain due to the mounting process can result in a nonzero quadrupolar frequency Ω_Q , though this splitting is likely to be on the order of 10 kHz for all isotopes.^{26,27} In addition, for nuclear sites near the surface of the particle where symmetry is broken, electric field gradients can result in large quadrupolar splittings. Nevertheless, the large majority of the nuclear spins detected in our experiments satisfy $\beta \gg 1$. These two conditions should allow our frequency sweep wave forms to adiabatically invert all four nuclear species.

VII. MODEL AND ESTIMATES

Modeling the magnitude and shape of the resonance peaks shown in Fig. 4 requires both knowledge of the spatial dependence of $B_{\text{total}}(\vec{r})$ and knowledge of the shape and position of the sample. Since $B_{\text{total}}(\vec{r})$ is strongly inhomogeneous, there is a specific region in space at which the magnetic resonance condition is met for each f_{RF} . Only spins near these positions are adiabatically inverted and therefore included in the MRFM detection volume. This so-called “resonant slice” is a shell-like region in space above the magnetic tip whose thickness is determined by the magnetic field gradient and the modulation amplitude $\Omega_{\text{RF}}/(2\pi)$ of the frequency sweeps. We can model this region more exactly using an effective field model for adiabatic rapid passage in the manner of Sec. IV of the supporting information in Degen *et al.*³ This model shows

that the spatial extent of the resonant slice can be described using a simple function:

$$\eta(\vec{r}) = 1 - \left(\frac{\gamma B_{\text{total}}(\vec{r}) - 2\pi f_{\text{RF}}}{\Omega_{\text{RF}}} \right)^2$$

$$\text{for } \gamma B_{\text{total}}(\vec{r}) - 2\pi f_{\text{RF}} < \Omega_{\text{RF}},$$

$$\eta(\vec{r}) = 0 \text{ for } \gamma B_{\text{total}}(\vec{r}) - 2\pi f_{\text{RF}} \geq \Omega_{\text{RF}}. \quad (5)$$

$\eta(\vec{r})$ is normalized to 1 for a nuclear spin positioned exactly in the middle of the resonant slice [$\gamma B_{\text{total}}(\vec{r}) = 2\pi f_{\text{RF}}$], signifying that this spin is fully flipped by the adiabatic passage waveform and contributes its full force to the MRFM signal. A slightly off-resonant spin with $1 > \eta(\vec{r}) > 0$ is partially flipped and contributes a fraction of its full force to the MRFM signal. Spins outside the resonant slice with $\eta(\vec{r}) = 0$ contribute no signal.

In order to calculate the σ_F^2 , we must therefore determine the intersection of the resonant slice with the sample for each f_{RF} . In addition, since the gradient varies throughout the resonant slice, equal numbers of nuclei at different positions in the slice contribute different forces to the final signal. Using (2), (4), and (5) we can then integrate over the volume of the sample to find the total MRFM force variance:

$$\sigma_F^2 = \int_S A \eta(\vec{r}) \left(\frac{\partial B_{\text{total}}(\vec{r})}{\partial x} \right)^2 na \frac{I(I+1)}{3} (\hbar \gamma)^2 dV, \quad (6)$$

where S is the sample volume and A is a constant—usually close to 1—which depends on the correlation time of the statistical spin polarization and the measurement detection bandwidth.

We determine $B_{\text{total}}(\vec{r})$ using a method employed in other recent MRFM experiments.^{3,25} First, we measure B_{total} at several different positions above the FeCo tip. The maximum value of f_{RF} for which a ^1H signal is obtained corresponds to the frequency where the resonant slice barely intersects the hydrocarbon surface layer closest to the FeCo tip. At this frequency $f_{\text{RF,max}}$, $B_{\text{total}}(\vec{r}_0) = \frac{2\pi}{\gamma} f_{\text{RF,max}}$ where \vec{r}_0 is the position of the hydrocarbon layer closest to the FeCo tip. Several such measurements of B_{total} at different \vec{r}_0 are then used to calibrate a magnetostatic model of the FeCo tip. We infer the shape of the FeCo tip from SEM images and we assume a magnetization of 10^6 A/m as in previous works.^{3,25} The geometrical parameters are fine-tuned in order to produce a field profile $B_{\text{tip}}(\vec{r})$ which agrees with the measured values of $B_{\text{total}}(\vec{r}_0) = |\mathbf{B} + \mathbf{B}_{\text{tip}}(\vec{r}_0)|$ for our known applied field \mathbf{B} . Our approximate model then gives us the ability to calculate both $B_{\text{total}}(\vec{r})$ and $\frac{\partial B_{\text{total}}}{\partial x}(\vec{r})$ at any position \vec{r} .

Given our approximate knowledge of the shape of the sample from SEM images such as Fig. 1, we can only estimate the sample volume S . The GaAs particle is modeled as a $2.4 \mu\text{m} \times 0.6 \mu\text{m} \times 0.1 \mu\text{m}$ rectangular solid with a 200-nm-thick layer of Pt on the end face. The hydrocarbon layer is modeled as a thin film on the surface of this solid. The dimensions of this sample are meant to match the cross-sectional size of the particle closest to the FeCo tip since this part of the sample contributes nearly all of the observed σ_F^2 . The back part of the sample, with larger cross-sectional area, contributes a vanishingly small σ_F^2 due to the rapid decrease in $\frac{\partial B_{\text{total}}}{\partial x}$ as a function of distance from the FeCo tip.

We then use our models for $\mathbf{B}_{\text{total}}(\vec{r})$ and S together in a numerical integration of (6) to calculate the dependence of σ_F^2 on f_{RF} . As shown in Fig. 6, the model reproduces the experimental data despite the approximate knowledge of the sample shape. Detailed structure within the peaks, however, is impossible to reproduce as it is often due to the nanometer-scale morphology not included in our idealized geometries. In fact, we can reproduce such large variations in the resonance peak shape by altering the details of the sample geometry used in our calculation. Prominent structure is particularly evident in resonances measured with small tip-sample spacings, where the magnetic field gradients are largest and small volumes of spins can contribute large force variances.

A thickness of 2 nm is chosen for the hydrocarbon layer in our model in order to produce a resonant σ_F^2 approximating our measurements. This thickness is consistent with previous measurements of such layers which estimated a thickness of approximately 1 nm.^{3,15} The small discrepancy could be due to differences in the surface properties of our sample including roughness and affinity to adsorption of hydrocarbons compared to previous samples.

Despite the approximate nature of our model for σ_F^2 , we can use it to make an order of magnitude estimate of the detection volume in our experiments. Using the parameters of each measurement, we can estimate the detection volume V_d as the sample volume intersecting the resonant slice, i.e., the volume in which $\gamma B_{\text{total}}(\vec{r}) - 2\pi f_{\text{RF}} < \Omega_{\text{RF}}$. The number of spins contained therein is then $N_d = naV_d$. In the case of the peak σ_F^2 from the hydrocarbon layer at $f_{\text{RF}} = 115.5$ MHz in Fig. 6, we calculate a $V_d = (40 \text{ nm})^3$ and $N_d = 6 \times 10^6$. For this spin ensemble the ratio of SNP to BNP is 0.20. Furthermore, we can estimate the sensitivity of this measurement since we know that SNR of our measurement increases with the square root of the averaging time. We calculated the SNR at each f_{RF} by dividing the measured σ_F^2 by the standard error of this measurement calculated as in Degen *et al.*¹¹ This error takes into account both the noise due to fluctuations in the cantilever motion, i.e., thermal noise and noncontact friction, and the noise due to the statistically polarized spin ensemble itself. Given the SNR of 14.4 achieved after 300 s of averaging, we estimate a measurement sensitivity equivalent to 7×10^6 ^1H spins/ $\sqrt{\text{Hz}}$. In general, the sensitivity of these measurements is limited by the mechanical fluctuations of the cantilever due to thermal noise and noncontact friction.

We can make similar calculations for the quadrupolar nuclei. The peak values of σ_F^2 shown in Fig. 4, however, do not represent the maximum attainable signal for each isotope. Due to the long averaging times required for these isotopes, position scans used to optimize the signal amplitude were not performed before these measurements. Approximate measurement positions were estimated based on the ^1H experiments resulting in smaller than optimal σ_F^2 . For ^{71}Ga , however, an x and y position scan was performed in order to find the optimal $\sigma_F^2 = 25 \text{ aN}^2$ at $f_{\text{RF}} = 34.95$ MHz. From this scan it was found that changes in position of less than only 50 nm resulted in signal loss of over a factor of 2, emphasizing the

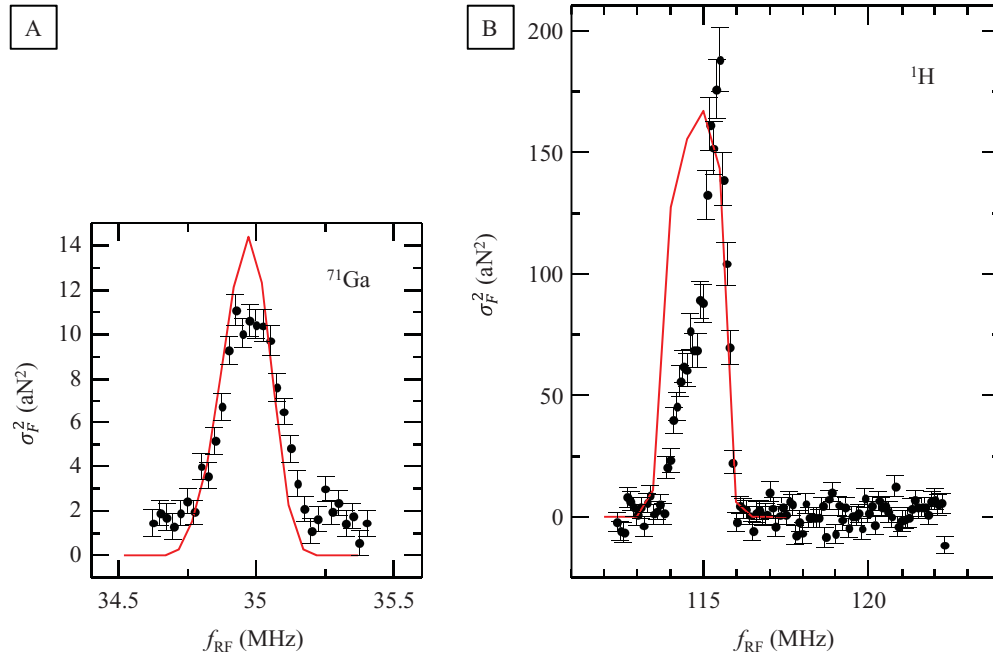


FIG. 6. (Color online) MRFM signal from the statistical polarization of (A) ^{71}Ga in the (B) ^1H from Fig. 4 along with the corresponding calculated signal from the our MRFM model. The sample position used in the model was matched to the experimentally set position within an error of 50 nm, likely due to experimental position drift during these long time scans. The position was fine-tuned within this error range to best match the measured signal.

importance of optimal alignment. This signal is in reasonable agreement with the maximum signal $\sigma_F^2 = 20 \text{ aN}^2$ calculated for the same parameters in our model. Using our model we can calculate $V_d = (260 \text{ nm})^3$ and $N_d = 2 \times 10^8$ for the ^{71}Ga signal plotted in Figs. 4 and 6, which is slightly shifted from the optimal position. In this case, we find $\text{SNP}/\text{BNP} = 0.14$ (see Table II). The corresponding sensitivity is estimated from the SNR of 15.4 after 600 s of averaging to be 2×10^8 ^{71}Ga spins/ $\sqrt{\text{Hz}}$. Similar calculations are not carried out for ^{69}Ga and ^{75}As , though sensitivity for these isotopes should be of the same order after a scaling factor equivalent to appropriate MRFM receptivity.

As discussed in Sec. V, the large difference in the sensitivity between ^1H and the quadrupolar nuclei is mostly due to the 200 nm Pt layer which forces the Ga and As moments into

TABLE II. Detection and sensitivity estimates for the ^1H and ^{71}Ga resonances plotted in Figs. 4 and 6 at $B = 2.65 \text{ T}$ and $T = 1 \text{ K}$.

| | ^1H (hydrocarbon layer) | ^{71}Ga (GaAs) |
|--|-------------------------------------|----------------------------|
| Sample-tip distance (nm) | 100 | 300 |
| Maximal $\frac{\partial B_{\text{total}}}{\partial x}$ at sample (T/m) | 5×10^5 | 8×10^4 |
| Maximal $ \mathbf{B}_{\text{tip}} $ at sample (T) | 0.10 | 0.03 |
| f_{RF} (MHz) | 115.5 | 34.95 |
| $\Omega_{\text{RF}}/(2\pi)$ (kHz) | 400 | 100 |
| N_d | 6×10^6 | 2×10^8 |
| V_d | $(40 \text{ nm})^3$ | $(260 \text{ nm})^3$ |
| SNP/BNP | 0.29 | 0.14 |
| Averaging time (s) | 300 | 600 |
| Sensitivity (spins/ $\sqrt{\text{Hz}}$) | 7×10^6 | 3×10^8 |

a region of far smaller magnetic field gradient than at the hydrocarbon layer. Future experiments should be designed such that this Pt layer, which is an artifact of the FIB mounting process, is not present. Without this intermediate layer, far better sensitivities should be achieved for the quadrupolar nuclei. Table III shows predicted sensitivities for ^{69}Ga , ^{71}Ga , and ^{75}As for a 100 nm spacing between the sample and the FeCo tip—without any intermediate layer. All other parameters are identical to those of the actual experiments. These extrapolations are based on positioning the Ga and As in the same position as the ^1H nuclei in our experiment. We make the assumption that the noise would be the same as that measured in the ^1H experiment.

TABLE III. Extrapolated detection and sensitivity estimates for the quadrupolar nuclei based on parameters achieved for ^1H at $B = 2.65 \text{ T}$ and $T = 1 \text{ K}$ in Table II.

| | ^{69}Ga (GaAs) | ^{71}Ga (GaAs) | ^{75}As (GaAs) |
|--|----------------------------|----------------------------|----------------------------|
| Sample-tip distance (nm) | 100 | 100 | 100 |
| Maximal $\frac{\partial B_{\text{total}}}{\partial x}$ at sample (T/m) | 5×10^5 | 5×10^5 | 5×10^5 |
| Maximal $ \mathbf{B}_{\text{tip}} $ at sample (T) | 0.10 | 0.10 | 0.10 |
| f_{RF} (MHz) | 27.9 | 35.1 | 19.8 |
| $\Omega_{\text{RF}}/(2\pi)$ (kHz) | 100 | 100 | 50 |
| N_d | 1×10^8 | 9×10^7 | 2×10^8 |
| V_d | $(210 \text{ nm})^3$ | $(210 \text{ nm})^3$ | $(200 \text{ nm})^3$ |
| SNP/BNP | 0.20 | 0.19 | 0.23 |
| Calculated σ_F^2 (aN^2) | 250 | 210 | 150 |
| Sensitivity (spins/ $\sqrt{\text{Hz}}$) | 1×10^8 | 9×10^7 | 3×10^8 |

VIII. CONCLUSION

The results presented here demonstrate our ability to detect nanometer-scale volumes of Ga and As nuclei using MRFM. Given the spin sensitivity extrapolated from our data and our model, the detection of III-V nanostructures such as nanowires or subsurface self-assembled InAs QDs should be possible. Self-assembled InAs QDs, for example, contain 10^5 – 10^7 nuclear spins, lie as close as 50 nm from the wafer surface, and could be attached to a cantilever using the FIB technique demonstrated here. Further improvements to the force sensitivity—most importantly for reducing measurement times—will be required in order to realize MRI in III-V materials with better than 100 nm resolution. The potential for subsurface, isotopically selective imaging on the nanometer

scale in III-V materials is a particularly exciting prospect since conventional methods such as SEM and TEM lack isotopic contrast.

ACKNOWLEDGMENTS

The authors thank Dr. Erich Müller from the Laboratory for Electron Microscopy at the Karlsruhe Institute of Technology for conducting the FIB process and Dr. Ben Chui for fabricating the cantilevers. We acknowledged support from the Canton Aargau, the Swiss National Science Foundation (SNF; Grant No. 200021 1243894), the Swiss Nanoscience Institute, and the National Center of Competence in Research for Quantum Science and Technology.

-
- ¹L. Ciobanu, D. A. Seeber, and C. H. Pennington, *J. Magn. Reson.* **158**, 178 (2002).
- ²M. Poggio and C. L. Degen, *Nanotechnology* **21**, 342001 (2010).
- ³C. L. Degen, M. Poggio, H. J. Mamin, C. T. Rettner, and D. Rugar, *Proc. Nat. Acad. Sci. USA* **106**, 1313 (2009).
- ⁴R. Verhagen, A. Wittlin, C. W. Hilbers, H. van Kempen, and A. P. M. Kentgens, *J. Am. Chem. Soc.* **124**, 1588 (2002).
- ⁵K. R. Thurber, L. E. Harrell, R. Fainchtein, and D. D. Smith, *Appl. Phys. Lett.* **80**, 1794 (2002).
- ⁶K. R. Thurber, L. E. Harrell, and D. D. Smith, *J. Magn. Reson.* **162**, 336 (2003).
- ⁷S. R. Garner, S. Kuehn, J. M. Dawlaty, N. E. Jenkins, and J. A. Marohn, *Appl. Phys. Lett.* **84**, 5091 (2004).
- ⁸H. J. Mamin, R. Budakian, B. W. Chui, and D. Rugar, *Phys. Rev. Lett.* **91**, 207604 (2003).
- ⁹H. J. Mamin, R. Budakian, B. W. Chui, and D. Rugar, *Phys. Rev. B* **72**, 024413 (2005).
- ¹⁰M. Poggio, C. L. Degen, C. T. Rettner, H. J. Mamin, and D. Rugar, *Appl. Phys. Lett.* **90**, 263111 (2007).
- ¹¹C. L. Degen, M. Poggio, H. J. Mamin, and D. Rugar, *Phys. Rev. Lett.* **99**, 250601 (2007).
- ¹²C. L. Degen, M. Poggio, H. J. Mamin, and D. Rugar, *Phys. Rev. Lett.* **100**, 137601 (2008).
- ¹³M. Poggio, H. J. Mamin, C. L. Degen, M. H. Sherwood, and D. Rugar, *Phys. Rev. Lett.* **102**, 087604 (2009).
- ¹⁴T. H. Oosterkamp, M. Poggio, C. L. Degen, H. J. Mamin, and D. Rugar, *Appl. Phys. Lett.* **96**, 083107 (2010).
- ¹⁵H. J. Mamin, T. H. Oosterkamp, M. Poggio, C. L. Degen, C. T. Rettner, and D. Rugar, *Nano Lett.* **9**, 3020 (2009).
- ¹⁶C. P. Slichter, *Principles of Magnetic Resonance* (Springer, Berlin, 1990), 3rd ed.
- ¹⁷B. W. Chui *et al.*, *Technical Digest of the 12th International Conference on Solid-State Sensors and Actuators (Transducers '03)* (IEEE Boston, MA, 2003), p. 1120.
- ¹⁸B. C. Stipe, H. J. Mamin, T. D. Stowe, T. W. Kenny, and D. Rugar, *Phys. Rev. Lett.* **87**, 096801 (2001).
- ¹⁹S. Kuehn, R. F. Loring, and J. A. Marohn, *Phys. Rev. Lett.* **96**, 156103 (2006).
- ²⁰J. L. Garbini, K. J. Bruland, W. M. Dougherty, and J. A. Sidles, *J. Appl. Phys.* **80**, 1951 (1996); K. J. Bruland, J. L. Garbini, W. M. Dougherty, and J. A. Sidles, *ibid.* **80**, 1959 (1996).
- ²¹Without damping by electronic feedback, the SNR of a thermally limited force measurement is given by the ratio of the signal force F_s to the thermal force acting on the cantilever $F_{th} = \sqrt{4k_B T k \Delta / (\omega_c Q)}$, where Δ is a measurement bandwidth much smaller than the cantilever bandwidth. This ratio is preserved even in the presence of electronic damping, since the damping reduces the amplitude and broadens the spectrum of any cantilever motion. Cantilever motion caused by either F_s or F_{th} is reduced equally and therefore the SNR and the force sensitivity (the size of the force required for an SNR of 1) remain unchanged. The spectral width of the cantilever motion, however, is broadened by damping, allowing for larger Δ and thus for the measurement of forces with faster correlation times.
- ²²E. Van Veenendaal, B. H. Meier, and A. P. M. Kentgens, *Mol. Phys.* **93**, 195 (1998).
- ²³P. T. Callaghan, *Principles of Nuclear Magnetic Resonance Microscopy* (Oxford University Press, Oxford, 1991), p. 174.
- ²⁴See Supplemental Material at <http://link.aps.org/supplemental/10.1103/PhysRevB.84.205328> for a description of the FIB process.
- ²⁵Fei Xue, P. Peddibhotla, M. Montinaro, D. P. Weber, and M. Poggio, *Appl. Phys. Lett.* **98**, 163103 (2011).
- ²⁶D. J. Guerrier and R. T. Harley, *Appl. Phys. Lett.* **70**, 1739 (1997).
- ²⁷M. Poggio and D. D. Awschalom, *Appl. Phys. Lett.* **86**, 182103 (2005).